Investigation of microstructure and mechanical performance of Ti6Al4V-ELI components produced by DMLS and EBM additive technologies in different geometries

E. Cerri, T. Rimoldi, R. Gabrini, L. Righi

A comparative study of the microstructural features of Ti6Al4V-ELI alloy components fabricated by Direct Metal Laser Sintering (DMLS) and Electron Beam Melting (EBM) were investigated. Samples had two different shapes, one cylindrical (CYL) and one parallelepiped (PAR). They were characterized in the build plane and in the two orthogonal planes by Optical Microscopy (OM) and Scanning Electron Microscopy (SEM) revealing a Basket-Weave (Widmanstätten) microstructure in each sample. X-ray Diffraction (XRD) spectra confirmed the presence of α and β phases with limited texturing. Quantitative processing of SEM images highlighted the presence of 10% β phase. All investigated samples satisfied related microhardness (ASTM F136-13) and tensile test (ASTM F2924-14) specifications; however, DMLS samples achieved the most isotropic mechanical properties. CYL-DMLS samples achieved the highest microhardness (404±4 HV0.5) and ultimate tensile strength (σ_{UTS} = 1155±50 MPa) maintaining outstanding elongation at 15±1%. By comparing the microstructure and mechanical behavior, it is evident that mechanical performance is strictly related to the fineness, homogeneity and size distribution of β domains dispersed in the α matrix.

KEYWORDS: TI6AL4V-ELI ALLOY – MICROSTRUCTURE – ADDITIVE MANUFACTURING – HARDNESS – XRAYS

INTRODUCTION

Additive Manufacturing (AM) is a promising technology that enables direct fabrication of near-net-shape (NNS) components. The majority of AM processes are based on powder bed fusion technology. This processing method consists of layer-by-layer 3D printing where the component is grown from powders comprising the raw material [1]. The procedure is based on selective and localized melting of powder layers that are several microns in thickness with either a laser [2] or electron beam [3]. This technology offers several useful advantages over traditional manufacturing processes [3,4], including: i) fabrication of complex components and functionally-graded structures, ii) achievement of NNS components employing different materials such as metals, ceramics and composites iii) direct tunability of the density and stiffness of components and iv) limitation of production waste by up to 85%.

Fast melting/solidification during beam scanning is nonetheless far from conditions of thermodynamic equilibrium. It has frequently been observed that the microstructure of components fabricated with AM assumes directional features leading to anisotropic properties. The dependence of mechanical performance on direction in final components should be avoided, tuned or at least controlled for industrial applications. It is therefore necessary to carefully study the impact of manufacturing conditions on the microstructure and mechanical properties. By exploiting experimental data, it is possible to formulate semi-empirical models with the aim of predicting relationships between the microstructure and performance [1].

The use of titanium and its alloys in industrial applications has expanded rapidly over recent decades due to its excellent physical and mechanical properties. Nowadays, titanium alloys are utilized in many fields including aerospace engineering [4], orthopaedic replacements [5], automotive components [6] and elsewhere when specific strength-to-weight ratio or high

Emanuela Cerri*, Tiziano Rimoldi, Riccardo Gabrini
Department of Engineering and Architecture, University of Parma, Parco Area delle Scienze 181/A, 43124 Parma, Italy
* Corresponding Author
Email: emanuela.cerri@unipr.it

Lara Righi
Department of Chemistry, Life Sciences and Environmental Sustainability, University of Parma, Parco Area delle Scienze 11/A, 43124 Parma, Italy - IMEM-CNR, Parco Area delle Scienze 37/A, 43124 Parma, Italy

corrosion resistance are required. All of these properties are directly related to the different crystalline structures of titanium. In particular, two different crystalline allotropic phases are observed [7]: a phase that is thermodynamically stable in ambient conditions, the α phase, and a second phase that is stable above 888°C, the β phase. The former has a hexagonal close-packed (hcp) structure while the latter exhibits a body-centred cubic (bcc) structure. The addition of α (Al, O, N) or β (Mo, Fe, V, Cr, Mn) stabilizers in proper amounts produces so-called α, α-β or β titanium alloys enabling fine tuning of several physical and mechanical properties such as density, strength, creep resistance and weldability [4].
Among known Ti-based alloys, Ti6Al4V is widely adopted for a broad range of applications. Ti6Al4V is an α-β alloy characterized by good workability and machinability together with an excellent combination of strength and ductility for working temperatures up to 400°C. Ti6Al4V-ELI is an extra-low interstitial (ELI) grade of Ti6Al4V [8]. The absence of interstitial elements (e.g. O_2, N_2, C) confers fabricated components with increased ductility and fracture toughness [4]. Ti6Al4V-ELI alloy and, more generally, ELI grade alloys are therefore usually employed for low-temperature and vacuum applications where the integrity of components under extreme conditions is a key factor.

In this work, cylindrical (CYL) and parallelepiped (PAR) Ti6Al4V-ELI samples are produced via Direct Metal Laser Sintering (DMLS) and Electron Beam Melting (EBM) in order to analyze the microstructural features and crystalline phases resulting from two different AM production processes. The microstructure morphology in the build plane and in both orthogonal planes is studied via optical microscopy (OM) and scanning electron microscopy (SEM). SEM image processing and XRD measurements are performed to provide valuable information regarding the relative quantities of α and β phases in both DMLS and EBM specimens. The anisotropy of the resulting mechanical properties is explored with Vickers microhardness and tensile tests at room temperature, with results correlated to the observed microstructural characteristics.

Experimental procedures

The Ti6Al4V-ELI alloy powder utilized for DMLS specimens was supplied by EOS GmbH (Germany), while that employed for EBM specimens was acquired from Arcam AB (Sweden). The nominal chemical compositions of both powders are reported in Table 1. Typical particle sizes were d_{50}=39±3micron and 45-80micron respectively for EOS and Arcam powders, respectively.

Tab. 1 – Nominal compositions (wt.%) of EOS and Arcam Ti6Al4V-ELI powders.

	Ti	Al	V	Fe	O	N	C	H
EOS	Bal.	5.5-6.75	3.5-4.5	<0.3	<0.2	<0.05	<0.08	<0.015
Arcam	Bal.	6.47	4.06	0.21	0.09	0.01	0.01	00.01

Samples were fabricated via DMLS with an EOS DMLS machine [9] and via EBM with an Arcam EBM machine [10]. In the former case, a 400 W ytterbium fiber laser beam with wavelength 1075 nm was focused to a spot size of 100 μm and translated over the powder surface at 1500-2000 mm/s following a checker board scanning strategy on. Layer thickness was 60 μm, while the entire process was performed in an Ar atmosphere with the build chamber heated to 80 °C. As-fabricated samples were subsequently heat treated in vacuum at 730 °C for 2 hours. The cooling process was carried out in two steps; at 520 °C for 95 minutes and then at RT for 20 minutes.
The EBM build was performed with a 60keV beam (up to 35 mA, diameter 150-250 μm) and a residual He pressure in the order of 10^{-3} mbar. In this case, layer thickness was 50 μm, while the build was performed with the build chamber held at 600 °C. The process was divided into two main steps; an initial pre-heating stage where the beam was scanned rapidly over the powder bed at up to 105 mm/s and a second stage where powder melting occurred as the beam was scanned at speeds of up to 103 mm/s. No post-fabrication thermal treatment was required for samples produced via EBM.
Schematics of each sample are given in Figure 1, together with the reference system employed.

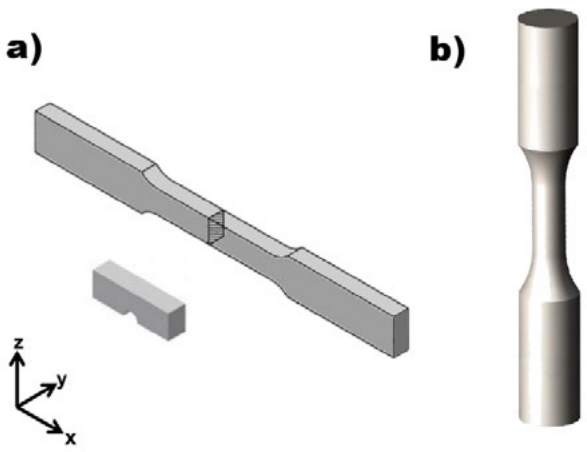

Fig. 1 – Schematic of samples: a) parallelepiped with 5x5 mm^2 section and 22 mm length, together with bar used for tensile tests and b) cylinder having gage length of 20mm, diameter of 6mm and total length of 100mm.

Figure 1a shows the PAR sample together with a typical tensile bar and Figure 1b shows the CYL sample. Tensile bars with constant gauge length section were built in the same job as the parallelepipeds; however, the four sample types (PAR-DMLS, PAR-EBM, CYL-DMLS and CYL-EBM) were produced in four different jobs. For DMLS production of PAR specimens, growth occurred along the Z direction (build axis), while in the case of EBM the build axis corresponded to the Y direction. For CYL specimens, the build axis corresponded to the Z direction for both DMLS and EBM. Reference to the different sample types will be made with the abbreviations reported in Table 2.

Tab. 1 – Nomenclature of investigated samples.

		Sample geometries	
		Cylinders	Parallelepipeds
Build technologies	DMLS	CYL-DMLS	PAR-DMLS
	EBM	CYL-EBM	PAR-EBM

Preparation for metallurgical analysis was carried out on three surfaces perpendicular to the X, Y and Z directions in correspondence with the reference system given in Figure 1. Surfaces were firstly ground with SiC abrasive paper and then polished with diamond paste. An etchant solution of 10% HF in deionized water was used to reveal the α-β microstructure, with immersion performed for 30-60 s. Analysis of the morphology was undertaken using a Leica DMi8C optical microscope equipped with image analyzer software and an FEG-SUPRA40 Zeiss SEM.

XRD patterns were acquired with a Thermo Scientific (Thermo ARL X'tra) instrument in a Bragg-Brentano θ-θ configuration equipped with a Cu (Kα, λ=1.542Å) radiation tube and a solid-state Si:Li detector that was cooled with a Peltier system. A typical diffraction pattern was collected with a step angle of 0.05° from 30 to 80 2θ degrees.

The relative quantities of α and β phases was evaluated quantitatively for PAR-DMLS and PAR-EBM samples with both Rietveld refinement of the XRD data (Jana2006 software) [11] and by processing SEM images in the Matlab environment.

The latter method was based on the analysis of SEM grey-scale images and provided the size distribution of β phase domains in terms of their equivalent diameters. As-acquired SEM images were firstly converted into binary images by introducing a grey-scale threshold separating white regions (β phase) from dark regions (α phase). Obtained black-and-white images were then cleaned by eliminating isolated pixels and voids located in dark or white regions. The area of each white region, together with its equivalent diameter, was subsequently determined. The frequency and area of each region was then counted to establish the size distribution of β phase domains along X, Y and Z axes.

A Leica VMHT hardness tester equipped with an x-y micrometric stage was employed for microhardness tests. 500 g was applied for 15 s on each of the three orthogonal planes using a random pattern of 10 points to determine the Vickers microhardness.

Tensile tests were carried out with a Zwick-Roell Z100 setup employing a relative strain rate of $8x10^{-3}$ s^{-1} to check the re-

sulting performance and allow comparison with other works in literature. Tests were repeated on up to 5 machined samples of each type (see section 2.2 and Figure 1).

Results and discussion

Etched PAR-DMLS and PAR-EBM samples were firstly examined with OM to investigate the α-β microstructure of the alloy. Typical OM images are shown in Figure 2, highlighting no preferential growth direction along X, Y and Z axes for both fabrication processes. Each direction is characterized by a typical Basket-Weave (Widmanstätten) structure [7] in which acicular plate-like areas of α phase (bright domains in Figure 2) are separated by β phase (dark domains in Figure 2).

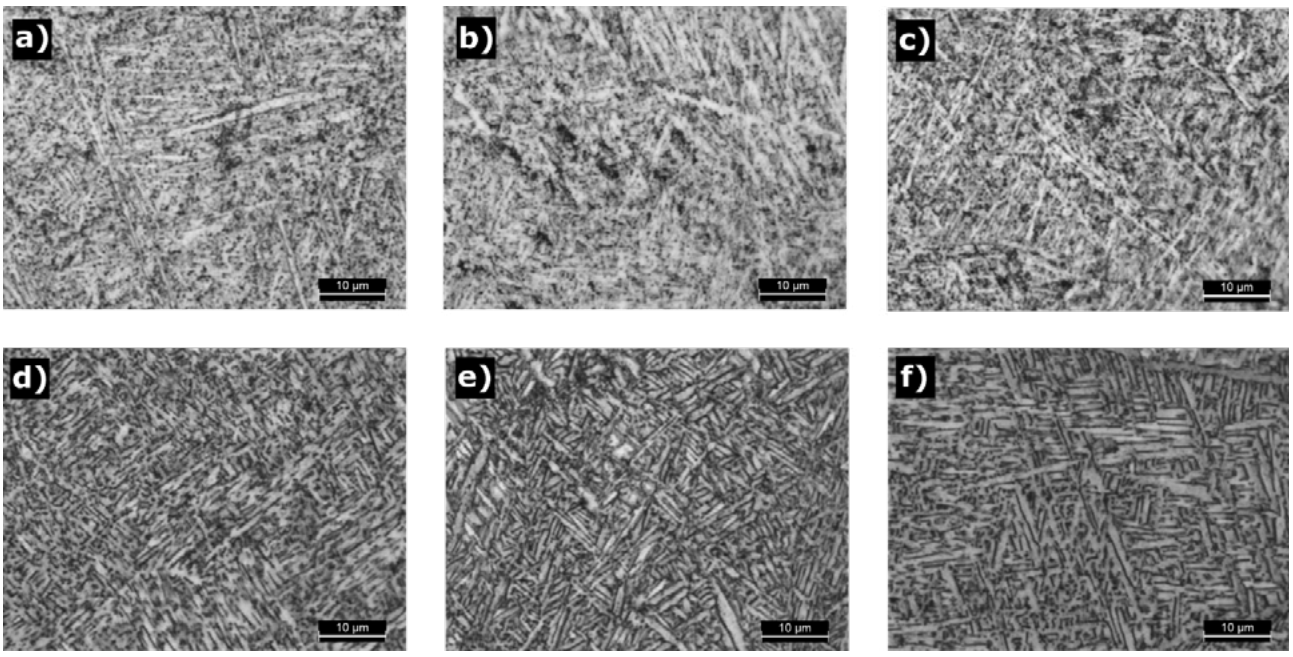

Fig. 2 – Optical images of PAR-DMLS (a, b and c) and PAR-EBM (d, e and f) samples acquired along the build direction (a and d), X axis (b and e) and perpendicular axis (c and f).

β domains present in the PAR-DMLS sample (parts Figure 2a, b and c) are small (<0.5 µm) and densely distributed, even after thermal treatment at 730 °C. Heat treatment was necessary to increase component toughness by removing, or at least reducing, the possible presence of α' martensite, which is promoted during the DMLS process due to the extremely rapid cooling rates involved (104-108 K/s [12]). The thermal treatment was therefore undertaken to promote the conversion α'→α, with transition typically taking place starting from small α' martensite domains until complete transformation took place.

As shown in Figure 2d, e and f, the PAR-EBM sample is characterized by a coarser microstructure exhibiting β domains about 1µm in size. This is essentially related to the slower cooling rate (<104 K/s [12]) experienced by the component during the EBM process. Such a condition is due to two main causes: i) the environment [3] in which EBM build takes place (low vacuum He atmosphere @ 10^{-3} mbar) and ii) the elevated temperature [10] maintained in the build chamber (up to several hundred °C). In this environment, formation of the metastable α' martensitic phase is hindered and thus post-build thermal treatment is not necessary.

With appropriately tuned process conditions, as was the case in the present study, the development of porosity or voids can be minimized. Consolidation steps normally used in standard powder metallurgy such as cold isostatic pressing (CIP), vacuum pressing (VHP) and hot isostatic pressing (HIP) could therefore be eliminated from the manufacturing procedure.

Alpha-beta structure

Further to microstructure morphology, the main concern surrounding the α-β nature of this alloy is related to the possible presence of residual martensitic α' phase that improves hardness but significantly worsens ductility [7]. The effectiveness of experimental procedures aimed at elimination of this undesired phase was checked with XRD measurements performed along the X, Y, and Z axes of each previously etched sample.

In pure titanium, the α phase is thermodynamically stable at ambient temperature while the β phase is stable above 888°C. The former has a hexagonal close-packed (hcp) structure while the latter has a body-centred cubic (bcc) structure [7]. Addition of α (Aluminium) and β (Vanadium) stabilizers within the titanium matrix allows maintenance of the ù phase at room temperature, constituting the so-called α-β alloy.

XRD spectra are reported in Figure 3 for both fabrication pro-

cesses. The α and β phases are clearly present in all acquired diffraction patterns. Spectra from the PAR-DMLS sample (Figure 3a) shows the presence of mostly α phase (long green lines) together with limited presence of β phase (short orange lines). Results for the PAR-EBM sample in Figure 3b are similar, with the intensity of β phase peaks low (X axis) or even negligible (Y and Z axes).

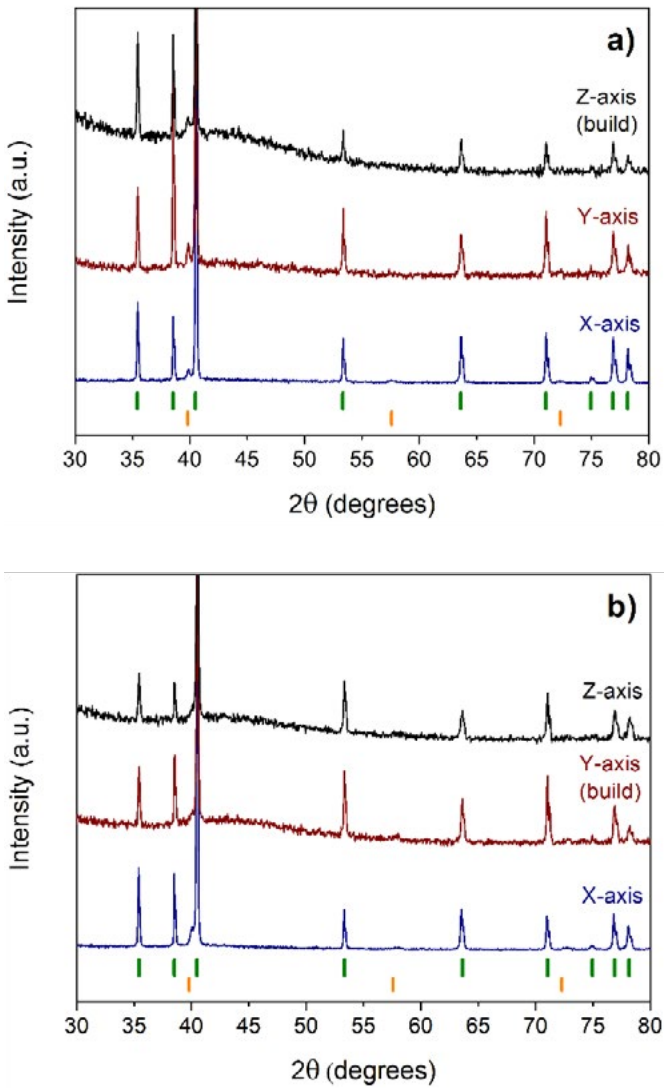

Fig. 3 – XRD spectra acquired along different axes for PAR-DMLS (a) and PAR-EBM (b) samples respectively. At the bottom of each graph the peak positions of α (long green lines) and β (orange short lines) phases are indicated.

Peaks are labelled according to Crystallographic Open Database CIF files for pure Ti-α (COD-ID 9016190) and Ti-β structures (COD-ID 9012924). Table 3 reports peak positions of α and β phases obtained by Rietveld refinement of the PAR-DMLS and PAR-EBM sample structures.

Tab. 3 – XRD indexing of α and β phases of Ti6Al4V-ELI samples (PAR-DMLS and PAR-EBM) performed by Rietveld refinement of the structures.

DMLS 2θ (grad)	EBM 2θ (grad)	hkl (α)	hkl (β)
35.42±0.09	35.38±0.11	1 0 0	
38.52±0.09	38.51±0.11	0 0 2	
39.8±0.3	40.0±0.2		1 0 1
40.49±0.09	40.46±0.11	1 0 1	
53.32±0.10	53.30±0.12	1 0 2	
57.6±0.3	57.9±0.3		0 0 2
63.59±0.11	63.53±0.13	2 -1 0	
71.02±0.12	70.98±0.14	1 0 3	
72.3±0.4	72.7±0.3		1 1 2
74.96±0.13	74.87±0.14	2 0 0	
76.88±0.13	76.81±0.14	2 -1 2	
78.16±0.13	78.08±0.14	2 0 1	

Peak sequences are consistent for both manufacturing processes. Moreover, Rietveld refinement highlights systematic shrinkage of unit cell parameters for both α and β phases (α phase with a=b=2.93 Å and c=4.67 Å, β phase with a=b=c=3.18 Å) compared to pure Ti (α phase with a=b=2.95 Å and c=4.68 Å, ù phase with a=b=c=3.28 Å). This is due to the reduced atomic radius of elements replacing Ti in the hexagonal (α phase) and cubic (β phase) structures. For instance, aluminium (α stabilizer) and vanadium (β stabilizer) have atomic radii of 1.43 Å and 1.35 Å, respectively, whereas the radius of titanium is 1.47 Å. The contraction effect is more pronounced for the β phase.

Rietveld refinement also allows estimation of the relative quantities of α and β phases. Results are shown in Table 4 for PAR samples produced with both fabrication techniques. Analyses performed on spectra collected along each direction (X, Y and Z) reveal that the β phase is below 5%. Unfortunately the β phase could not be accounted for in refinement along the Y and Z directions of the PAR-EBM sample due to overlap between the weak peak at 40° and the main reflection at 40.5° related to the α phase, as seen in Figure 3b. Tentative peak fitting provided unreliable results relating to the relative phase quantities.

Tab. 4 – Relative abundances of α and β phases obtained by both Rietveld refinement of the XRD spectra shown in Figure 3 and image processing of SEM images (Figure 4, a and b).

		Rietveld refinement		SEM image processing	
		α (%)	β (%)	α (%)	β (%)
PAR-DMLS	x	97	3	94	6
	y	96	4	94	6
	z-build	97	3	95	5
PAR-EBM	x	96	4	89	11
	y-build	100	nd*	90	10
	z	100	nd*	90	10

*Evaluation was not possible due to a negligible β phase signal (for more details refer to Figure 3b and related discussion)

A complementary approach for estimation of the phase distribution was based on measurement of the lateral extension of β phase domains in a pre-defined area of electron microscopy images. SEM measurements were performed on etched surfaces of PAR-DMLS and PAR-EBM samples to evaluate the characteristic size distribution of β domains. This approach overcame the aforementioned limits of XRD but, in turn, provided an intrinsically local evaluation of the phase quantities.

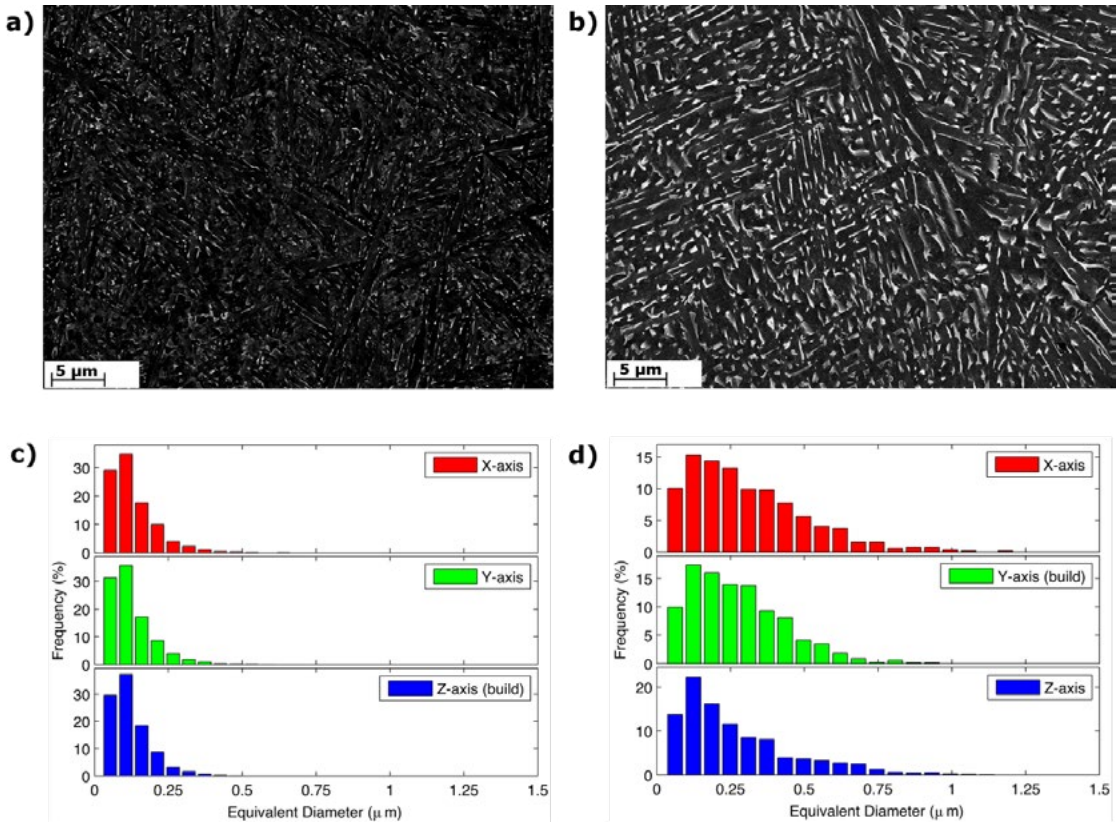

Fig. 4 – SEM images acquired along the build direction of PAR-DMLS (a) and of PAR-EBM (b) samples together with the equivalent diameter of the β domains in X, Y and Z directions (c, PAR-DMLS and d, PAR-EBM).

Two typical SEM images of PAR-DMLS and PAR-EBM samples along the build axis are reported in Figure 4a and b, respectively. As a consequence of the nature of SEM contrast, the dark flat area represents the α phase whilst the bright regions indicate the presence of β domains. Magnification was chosen to optimize statistics and resolution. In agreement with OM measurements, the PAR-DMLS sample microstructure is densely distributed, with equivalent diameter distributions of β domains (Figure 4c) sharpened around 150 nm in all investigated directions. On the contrary, the microstructural features of the PAR-EBM sample are different; the β phase domains are coarse and widely spaced. The equivalent diameter distribution presented in Figure 4d presents strong broadening towards larger values, together with a slight shift of the maximum with the mean size of β domains rising to 300 nm. Calculated areas are given in Table 4. The amount of β phase is almost 5% in each plane (X, Y and Z) for the PAR-DMLS sample, while this value reaches 10% for the PAR-EBM sample, in agreement with the literature [13].

There is marked inconsistency between results obtained via Rietveld refinement of XRD data and those obtained with SEM image processing (Table 4), especially for the PAR-EBM sample. The reason for this discrepancy is not related to the different sizes of the investigated areas, in the order of mm^2 for XRD and hundreds of μm^2 for SEM images, nor inhomogeneity of the studied microstructures. The reason is instead likely related to texturing of the microstructure together with the limited crystallinity of β phase domains.

The Rietveld method is based on the assumption that crystals are randomly oriented with no preferential direction. During DMLS and EBM, however, grains constituting the produced material may grow preferentially along favored directions leading to texturing [14, 15]. In the present case, the intensity of XRD peaks (Figure 3) indicates moderate texturing of grains in both PAR-DMLS and PAR-EBM samples. At the same time, broadening of the detected β phase peaks (Figure 3) clearly indicates poor crystallinity of the β domains and, as a consequence, limited contribution to the diffracted intensity. The lack of reliable XRD results relating to determination of the ß phase has been discussed by Krakhmalev et al. [16], who

showed that TEM and XRD investigations failed to detect the β phase. In both diffraction techniques, fine dispersion of β grains in a matrix prevents correct quantitative evaluation of the secondary phase. The limited quantity and low crystallinity of the β phase consequently lead to underestimation of the relative phase quantity obtained via XRD analysis. Conversely, underestimations can easily be avoided in SEM image processing because it is possible to directly discriminate the two phases through their different grey tones.

Mechanical properties

PAR-DMLS and PAR-EBM samples were subjected to microhardness and tensile tests with the aim of evaluating their static mechanical properties. Results relating to Vickers microhardness tests are presented in Figure 5.

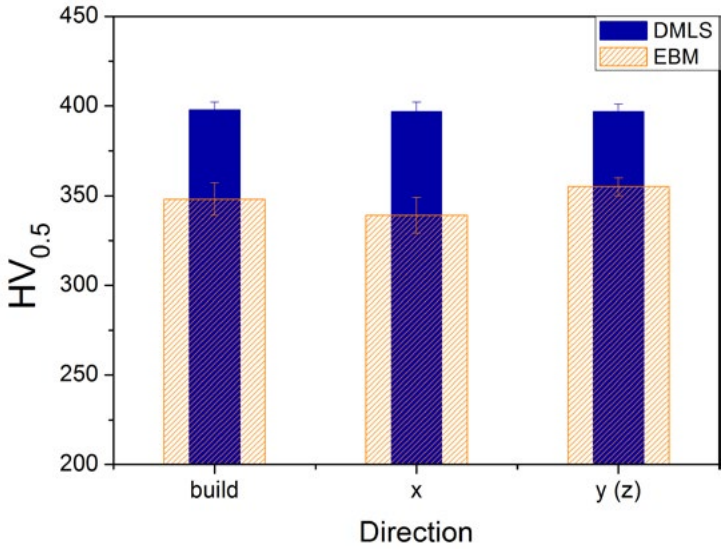

Fig. 5 – Comparison between PAR-DMLS and PAR-EBM Vickers microhardness along the three orthogonal directions. The build direction for PAR-DMLS samples was Z, while for PAR-EBM was Y. Data labelled Y for PAR-DMLS is therefore superimposed on data labelled Z for PAR-EBM.

The hardness of PAR-DMLS samples (blue columns) was consistently higher than that of PAR-EBM samples (orange columns); 398±4 HV and 355±5 HV, respectively. The surface of each investigated specimen displayed good HV isotropy and homogeneity, especially for PAR-DMLS specimens due to the post-production heat treatment. HV values are in agreement with ASTM F136-13 [17] technical specifications (300-340 HV) for a typical Ti6Al4V-ELI alloy and demonstrate that both DMLS and EBM methods are efficient fabrication processes.

Values obtained during tensile tests are reported in Table 5 for PAR-DMLS and PAR-EBM samples.

Tab. 5 – Mechanical parameters of PAR-DMLS and PAR-EBM samples compared to technical specifications given in ASTM-F 2924-14 [17].

	PAR-DMLS	PAR-EBM	ASTM F2924-14
σ_{UTS} (MPa)	1140±35	1035±34	895
σ_{YS} (MPa)	1080±30	950±35	825
ε (%)	15±1	17.5±1.5	10

The ultimate tensile strength (σ_{UTS}), yield strength (σ^{YS}) and percentage elongation (ε) are far above ASTM F2924-14 standard specifications [18] in all cases. As with the Vickers microhardness, a higher yield strength was observed for PAR-DMLS samples. The linear relationship between σ_{YS} and HV remained valid for both manufacturing processes, with σ_{YS}/HV ratios of 2.71±0.06 and 2.68±0.05 for PAR-DMLS and PAR-EBM samples, respectively, which were not markedly different from the common value of 3.27 [19].

Shape comparison

It is well known that specimen shape and building strategy can

affect overall performance of components produced with additive manufacturing technologies. The investigation was therefore extended to consider a different geometry comprising cylindrical samples built along the Z axis (Figure 1) via DMLS and EBM, with the same thermal treatment performed in the former case as was employed for parallelepiped specimens.
The microstructure of the obtained samples was investigated with OM after polishing and etching in line with the procedure described in the 'materials and methods' section. For the purpose of isolating the effects of geometry, comparative analysis was carried out by considering the building axis only. The obtained results were not affected by elements related to morphology of the produced samples. Figure 6 shows optical images of CYL-DMLS and CYL-EBM samples. It is possible to observe a Basket-Weave (Widmanstätten) microstructure similar to that found in parallelepiped samples (Figure 2), where the α matrix (bright, Figure 6) is alternated with β phase domains (dark, Figure 6).

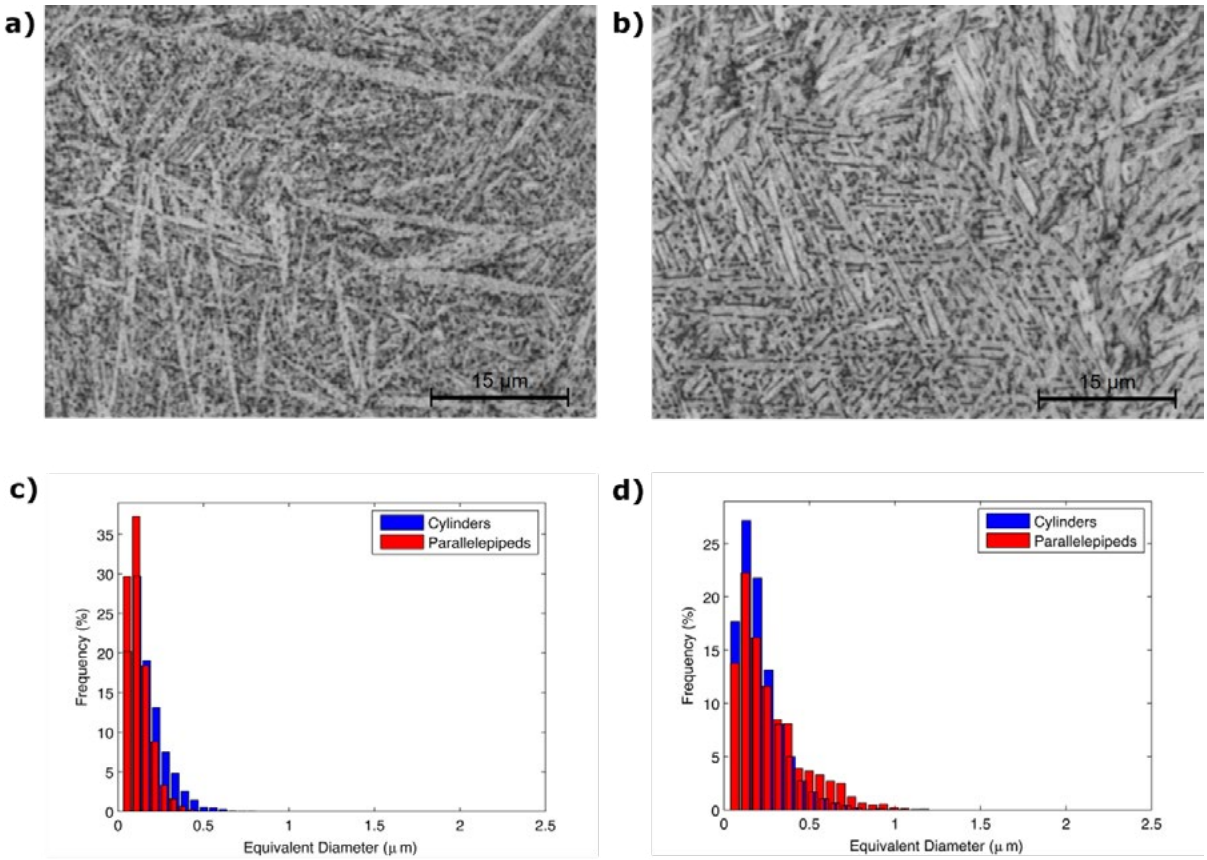

Fig. 6 – Details acquired along the build direction of CYL-DMLS and CYL-EBM samples: optical images of the fromer (a) and latter (b), respectively. In panels c and d the equivalent diameter distributions extrapolated from SEM images for both sample geometries (blue, cylinders and red, parallelepipeds) are compared.

A comparison of the size distributions of β domains for cylindrical and parallelepiped samples, calculated based on SEM images taken along the built axis, is given in Figure 6c and d. The average equivalent diameter of β domains is around 200nm for the CYL-DMLS sample, while the equivalent diameter is approximately 300nm for the CYL-EBM sample. Average values are similar in both cases; however, the distribution (Figure 6c, blue bars) is broadened towards larger dimensions for the CYL-DMLS sample. An opposing trend can be observed for the CYL-EBM sample (Figure 6d, blue bars), where the distribution is sharpened around the average value. In contrast to observations relating to parallelepiped samples, the CYL shape does not confer large differences in microstructure (see Figure 6a and b).
The mechanical properties of cylindrical samples produced with both DMLS and EBM are summarized in Table 6.

Tab. 6 – Mechanical properties of cylindrical samples build with DMLS and EBM technologies.

	CYL-DMLS	CYL-EBM
Vickers microhardness(HV0.5)	404±4	366±7
σ_{UTS} (MPa)	1155±50	1066±45
σ_{YS} (MPa)	1079±20	968±25
ε (%)	14.8±0.5	16.4±0.6

In both cases, mechanical properties are in agreement with standard specifications given in ASTM F2924-14 (tensile tests [18]) and ASTM F136-13 (hardness tests [17]). The tensile strength and hardness of CYL-DMLS samples (Table 6) agree with those of PAR-DMLS samples (Table 5 and Figure 5) and are consistently higher than those of samples built with EBM technology.

A series of suitable strategies for strengthening and hardening can be adopted to enhance the mechanical performance of α-β titanium alloys such as Ti-6Al-4V-ELI. The presence of interstitial elements (oxygen, nitrogen, hydrogen and carbon) or the chemical substitution of elements such as aluminium or tin can play the role of solid-solution strengtheners (SSS) into the α phase. Other efficient methods include microstructural features, grain size, texturing and heat treatments [20].

Because of the ELI grade of the chosen titanium alloy, PAR and CYL samples produced during experiments had the same nominal compositions (Table 1), for which the role of interstitial elements was negligible. Secondly, the role of substitutional elements was equivalent for the same reason.

The superior performance of samples produced via DMLS compared to those produced via EBM in terms of hardness and strength (Table 6) can therefore be attributed to the different heat treatments employed during production, specifically the faster cooling rate during DMLS (104-108 K/s [12]) compared to EBM (<104 K/s [12]). In DMLS, the speed of cooling firstly promotes the formation of a small and densely distributed microstructure comprising β phase domains embedded in the α′ phase matrix. Subsequently, heat treatment at 730 °C induces the α′→α phase conversion where the resulting α phase retains the morphology of the α′ domains. Thus, both the finer microstructure (Figure 2) compared to EBM samples, combined with the possible presence of residual α′ phase dispersed in the α matrix (below the XRD detection limit), could provide a reasonable explanation for the improved hardness and strength performance.

In relation to samples produced via EBM, tensile test results for CYL-EBM samples (Table 6) are slightly better than those for PAR-EBM samples (Table 5). The main difference between the two different shaped samples is instead related to the average microhardnesses, with CYL-EBM samples being 20 points higher than PAR-EBM samples. This behavior is due to differences in microstructure between the two samples. As mentioned previously, finer microstructure promotes more efficient mechanical performance. In the case of CYL-EBM samples (Figure 6), the size distribution of β phase domains sharpens around smaller equivalent diameters resulting in a finer microstructure and therefore higher microhardness; 366±7 HV0.5 compared to 348±8 for PAR-EBM samples.

Conclusion

DMLS and EBM additive manufacturing technologies have been compared in relation to production of cylindrical (CYL) and parallelepiped (PAR) Ti6Al4V-ELI specimens. In the case of DMLS, post-production heat treatment at 730 °C for 2 hours was necessary to reduce the hexagonal α′ martensitic phase originating from rapid cooling (up to 108 K/s) to below the XRD detection limit.

Optical microscopy and scanning electron microscopy highlighted Basket-Weave (Widmanstätten) microstructures for both geometries, typical of TI6Al4V-ELI α-β titanium alloy.

XRD investigation confirmed the presence of α and β phases and limited texturing for PAR samples. In turn, SEM image processing revealed α-β relative quantities of around 10%. The α/β ratio in EBM samples was found to double compared to DMLS technology. Average equivalent diameters of β domains for CYL geometry were found to be 200nm and 300nm for DMLS and EBM, respectively. Such values were similar to those of PAR samples; 150 nm and 300 nm, respectively. The domain distribution of CYL-DMLS samples was nonetheless broadened towards larger dimensions compared to PAR-DMLS samples, while an opposing trend was observed for CYL-EBM samples.

In relation to mechanical properties, all samples satisfied ASTM F136-13 microhardness and ASTM F2924-14 tensile test technical specifications for a typical Ti6Al4V-ELI alloy. In particular, CYL-DMLS achieved the best performance, with average Vickers microhardness values of up to 404±4 HV and an ultimate tensile strength, σUTS, of up to 1155±50 MPa, while maintaining an outstanding elongation of 15±1%.

It is therefore possible to infer that the superior mechanical performance of DMLS samples compared to EBM samples for both tested geometries is related to the fineness, homogeneity and size distribution of β domains in the α matrix.

Acknowledgments

The authors would like to acknowledge BEAM-IT (Fornovo, Parma, Italy) for providing samples that were investigated in this work.

REFERENCES

[1] W.E. Frazier, Metal Additive Manufacturing: A Review, J. of Materi. Eng. and Perform. 23, (2014) 1917-1928.

[2] D.D. Gu, W. Meiners, K. Wissenbach and R. Poprawe, Laser additive manufacturing of metallic components: materials, processes and mechanisms, Int. Mater. Rev. 57, (2012) 133-164.

[3] L.E. Murr, S.M. Gaytan, D.A. Ramirez, E. Martinez, J. Hernandez, K.N. Amato, P.W. Shido, F.R. Medina and R.B. Wicker, Metal Fabrication by Additive Manufacturing Using Laser and Electron Beam Melting Technologies, J. Mater. Sci. Technol. 28, (2012) 1-14.

[4] Matthew J. Donachie Jr., Titanium A Technical Guide, second ed., ASM International, Materials Park, Ohio, 2000, pp. 5-11.

[5] S.L. Sing, J. An, W.Y. Yeong and F.E. Wiria, Laser and Electron-Beam Powder-Bed Additive Manufacturing of Metallic Implants: A Review on Processes, Materials and Designs, Mater. Design. 34, (2016) 369-385.

[6] C. Leyens and M. Peters, Titanium and Titanium Alloys: Fundamentals and Applications, John Wiley & Sons, Koln, Germany, 2003.

[7] Matthew J. Donachie Jr., Titanium - A Technical Guide, second ed., ASM International, Materials Park, Ohio, 2000, pp. 13-24.

[8] ASTM International, ASTM F3001-14: Standard Specification for Additive Manufacturing Titanium-6 Aluminum-4 Vanadium ELI (Extra Low Interstitial) with Powder Bed Fusion, http://www.astm.org/Standards/F3001.htm, 2014 (accessed 5 June 2017).

[9] EOS e-manufacturing solutions, Systems and Solutions for Metal Additive Manufacturing, http://www.eos.info (accessed 6 June 2017).

[10] Arcam AB CAD to Metal, Cost-efficient Additive Manufacturing Solutions, http://www.arcam.com (accessed 6 June 2017).

[11] V. Petricek, M. Dusek and L. Palatinus, Crystallographic computing system JANA2006: General features, Z. Kristallogr. 229, (2014) 345-352.

[12] D. Herzog, V. Seyda, E. Wycisk and C. Emmelmann, Additive manufacturing of metals, Acta Mater. 117, (2016) 371-392.

[13] Matthew J. Donachie Jr., Titanium - A Technical Guide, second ed., ASM International, Materials Park, Ohio, 2000, pp. 102-105.

[14] J.J. Lewandowski and M. Seifi, Metal Additive Manufacturing: A Review of Mechanical Properties, Annual Rev. Mater. Res. 46, (2016) 151-186.

[15] C. de Formanoir, S. Michotte, O. Rigo, L. Germain and S. Godet, Electron beam melted Ti–6Al–4V: Microstructure, texture and mechanical behavior of the as-built and heat-treated material, Mat. Sci. Eng. A-Struct. 652, (2016) 105-119.

[16] Krakhmalev P., Fredriksson G., Yadroitsava I., Kazantseva N., du Plessis A. and Yadroitsev I., Deformation behavior and microstructure of Ti6Al4V manufactured by SLM, Physics Procedia 83, (2016) 778-788.

[17] ASTM International, ASTM F136-13: Standard Specification for Wrought Titanium-6Aluminum-4Vanadium ELI (Extra Low Interstitial) Alloy for Surgical Implant Applications (UNS R56401), https://www.astm.org/Standards/F136.htm, 2013 (accessed 5 June 2017).

[18] ASTM International, ASTM F2924-14: Standard Specification for Additive Manufacturing Titanium-6 Aluminum-4 Vanadium with Powder Bed Fusion, https://www.astm.org/Standards/F2924.htm, 2014 (accessed 5 June 2017).

[19] George F. Vander Voort, Metallography - Principles and Practice, ASM International, Materials Park, Ohio, 2000, pp. 334-409.

[20] Matthew J. Donachie Jr., Titanium - A Technical Guide, second ed., ASM International, Materials Park, Ohio, 2000, pp. 99-102.